Computers and Electrical Engineering 000 (2017) 1–17

Contents lists available at ScienceDirect

Computers and Electrical Engineering

journal homepage: www.elsevier.com/locate/compeleceng

# A new modified neutrosophic set segmentation approach☆

Eser Sert

*Kahramanmaraş Sutçu Imam University, Faculty of Engineering and Architecture, Department of Computer Engineering, 46400 Kahramanmaras, Turkey*

ARTICLE INFO

*Article history:*
Received 1 July 2016
Revised 19 January 2017
Accepted 20 January 2017
Available online xxx

*Keywords:*
Neutrosophic set
Neutrosophy
Otsu's method
Fuzzy C-means
3D segmentation
3D modeling
Entropy norm
Clustering

ABSTRACT

Segmentation is paramount to 3D video systems employing multi-view video-plus-depth data (MVD) to implement free-viewpoint navigation and comfortable 3D viewing, modeling, and comprehension. The Neutrosophic Set (NS) concept relies on the neutrosophy theory dealing with structures, and it focuses on the origin, scope, and nature of neutralities. NS used in this study is norm-entropy-based, and it is called Modified Neutrosophic Set Segmentation (MNSS). 3D modeling method via MNSS (3DMM_MNSS) proposed in this study improves the quality of single object 3D modeling through an NS stratagem called MNSS. 3DMM_MNSS is compared with 3D modeling method via OATS (3DMM_OATS) and with the 3D modeling method via FCMS (3DMM_FCMS). MNSS improves the quality of 3D modeling and prevents the problems arising from the depth map imprecision in terms of Figure of Merit (FOM), the Peak Signal-to-Noise Ratio (PSNR), and the Uniformity Measure (UM) as performance metrics.



## 1. Introduction

Since the images taken with classic cameras are 2D, it may sometimes be difficult to detect the depth information of the target object. Thanks to the advancements in 3D modeling technology, objects can be displayed with better quality and as close to their actual sizes on electronic systems when compared to 2D. At the same time, image processing algorithms can also be applied on the obtained images. Because of these advantages, 3D imaging technologies are commonly used in the defense industry, medicine, education, machinery and many other fields [1]

The notion of the Neutrosophic Set (NS) is based on the neutrosophy theory – which is a new branch of Philosophy - and deals with the scope, origin, and nature of the neutralities [2]. Successful results can be obtained by using NS in image processing applications such as thresholding and segmentation. Problems that are not dealt with fuzzy logic can be resolved by using the NS [3]. Because of these properties, effective results are obtained in image processing applications with NS.

Segmentation is one of the most important processes in pattern recognition, 3D modeling and computerized vision systems. Segmentation can be defined as objects divided into parts composing them. Modified Neutrosophic Set Segmentation (MNSS), Fuzzy C-Means Segmentation (FCMS) and Otsu's Adaptive Thresholding-based Segmentation (OATS) are used in this study. There are few studies on NS-based segmentation in the literature. Guo and Cheng [4] proposed a new method for the NS-based image segmentation. Zhang et al. [5] proposed Neutrosophic approach for image segmentation. Koundal et al. [6] used spatial information with clustering and level-sets for the segmentation of thyroid nodule. Alsmadi [7] used hybrid Fuzzy C-Means and Neutrosophic approach for segmentation.

☆ Reviews processed and recommended for publication to the Editor-in-Chief by Associate Editor Dr. G. Botella.

*E-mail addresses:* esersert@ksu.edu.tr, esersert80@gmail.com

http://dx.doi.org/10.1016/j.compeleceng.2017.01.017
0045-7906/

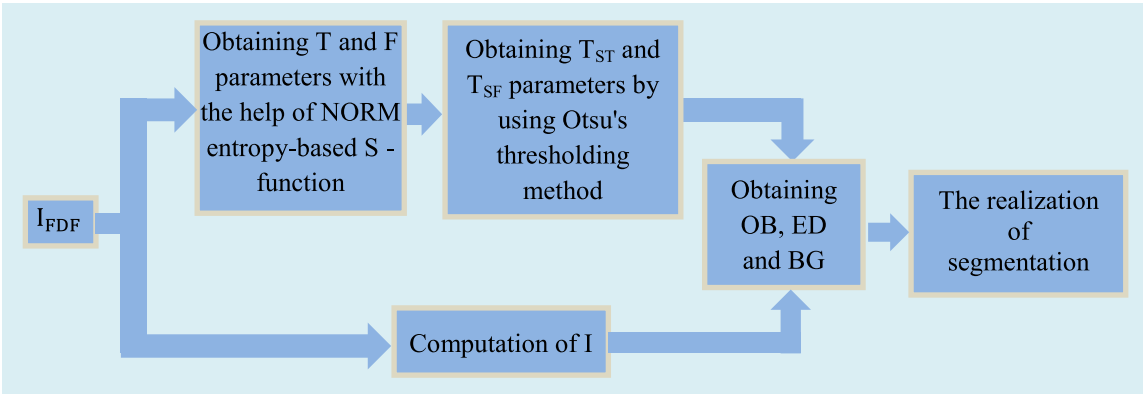


**Fig. 1.** The flow diagram of NS - based segmentation.

The segmentation types used for 3D point cloud are divided into five groups as edge-based methods, region-based methods, attribute-based methods, model-based methods and graph-based methods [8]. Previous studies and experiments have shown that the segmentation directly on 3D point cloud extends the segmentation duration, causes noise interference and also many other problems [9].

The depth map is an image which changes depending on the distance of the surface from a particular viewpoint [10]. A 3D model of the object is obtained by combining depth map and the original image of the object to be modeled. In this study, depth map images of 20 boxes used for experimental purposes were obtained via Structured Light (SL) system [1] designed by us. Experimental studies demonstrate that factors such as 3D modeling technology, ambient lighting and reflection can distort depth map due, which leads to problems in 3D modeling. In this study, segmentation of the original image to be modeled is initially performed by using MNSS. Then, it is aimed to obtain an ideal 3D model by 3D modeling method via MNSS (3DMM_MNSS).

FCMS is a commonly used fuzzy clustering method. It minimizes the criterion function based on the similarities of elements and cluster centers [11]. FCMS algorithm is quite efficient in noiseless image [11], while its performance decreases in noisy images. The other method, OATS [12], is one of the most commonly used approaches and is a clustering-based method. This method, however, lacks the accurate calculation of threshold value when histogram displays unimodal or close-to-unimodal distribution [13]. In this study performance of MNSS method is compared with FCMS [11,14] and OATS [12,13] algorithms.

The rest of the paper is organized as follows: theoretical background and segmentation methods are described in Section 2 and 3. 3D modeling is analyzed in detail in Section 4. Experimental studies are presented in Section 5 and concluding remarks are presented in the last section.

## 2. Theoretical background

### 2.1. Neutrosophic sets

A new approach introduced by Florentine Smarandache, neutrosophy theory is a powerful technique which has recently become popular [15]. Neutrosophy is based on neutrosophic logic, neutrosophic probability, neutrosophic set, and neutrosophic statistics [3]. In Neutrosophic logic, ⟨A⟩ defines an event, while ⟨Anti-A⟩ is the opposite of ⟨A⟩. ⟨Neut-A⟩ variable, based on neutrosophic theory, is different from ⟨A⟩ and ⟨Anti-A⟩, and is used to denote indeterminate situations [15]. An element of neutrosophic theory, neutrosophic set (NS), analyzes the origin, nature and scope of neutralities. It can be also associated with other disciplines. In NS theory, situations are classified and analyzed under three groups as “True”, “False” and “Indeterminacy”. The result of a match, stock exchanges or weather forecast can be given as examples of indeterminacies in daily life [16]. Since NS is a successful tool in solving indeterminacy problems and there can be indeterminate situations in images, it has recently been used in image processing applications such as segmentation, edge detection, thresholding etc.

### 2.2. Neutrosophic image

Preprocessing of the image is performed at the beginning of the NS-based segmentation process. Then, $I_{FDF}$, which is the pre-processed image, is processed and converted into Neutrosophic subsets in the form of True T, Indeterminacy I, and Falsehood F. In these three subsets, there are objects (OB) in *T*, background (BG) in *F* and regions that contain edges and uncertainties (ED) in the grayscale version of the original image in *I* [5]. Then, OB, BG, and ED regions are found by using T, I, and F. The segmentation is carried out in the final step. MNSS process is demonstrated in Fig. 1.

Please cite this article as: E. Sert, A new modified neutrosophic set segmentation approach, Computers and Electrical Engineering (2017), http://dx.doi.org/10.1016/j.compeleceng.2017.01.017


a) Original image b) Gray original image c) $I_{FDF}$ image

**Fig. 2.** Original image and images obtained during filtering.

*2.2.1. Preprocessing*

Fractional calculus [17–19] has been recently used in various applications and yielded successful results. Fractional Filter is used to preprocess an image. In this step, the fractional derivative developed by Khanna and Chandrasekaran [17] is used to adaptively improve the original image depending on the statistics of the image. Various filters are used in the study, and the fractional derivative filter was preferred in this study because it yielded the best result. A multi-directional mask is used in this approach for image contrast improvement. Mask co-efficient is determined based on Grunwald Letnikov (GL) definition [17]. GL is defined as follows [17,19]:

$$lim_{h\to 0} b^{-v}(-1)^m \sum_{m=0}^{n-1} \frac{\Gamma\ (v+1)}{\Gamma\ (m+1)\Gamma\ (v-m+1)} i(t-mh), \tag{1}$$

where i(t) process is between [a t], v ∈ R (it may be a fraction) is calculated as b=(t−a) / n and corresponds to step size. Γ(x) is equal to (x-1)! and gamma function of Eq. (1). The method details can be found in [17]. Original image shown in Fig 2(a) is converted to gray format at the beginning of pre-processing, and the filter is applied to the converted image to obtain Fractional Derivative Filter Image ($I_{FDF}$) as shown in Fig. 2(c).

*2.2.2. Obtaining T subset with S-function*

The T subset is obtained as a result of applying the S-function with $ref_1$, $ref_2$ and $ref_3$ [5,20] parameters to $I_{FDF:}$

$$T(i,j) = S - function(I_{FDF}(i,j); ref_1; ref_2; ref_3), \tag{2}$$

The *T* subset related to the *S*-function is defined by Eq. (3) [5,20].

$$\mathrm{T(i,j)}=\begin{cases} 0, & I_{FDF}(i,j) \le \mathrm{ref}_1, \\ \dfrac{(I_{FDF}(i,j)-ref1)^2}{(ref2-ref1)(ref3-ref1)}, & ref_1 \le I_{FDF}(i,j) \le \mathrm{ref}_2, \\ 1-\dfrac{(I_{FDF}(i,j)-ref3)^2}{(ref3-ref2)(ref3-ref1)}, & \mathrm{ref}_2 \le I_{FDF}(i,j) \le \mathrm{ref}_3, \\ 1, & I_{FDF}(i,j) \ge \mathrm{ref}_3, \end{cases} \tag{3}$$

Fig. 3 illustrates the S-function, where the parameters $ref_1$, $ref_2$ and $ref_3$ determine its shape. $ref_1$ corresponds to the peak value at the far left of the histogram, and $ref_3$ corresponds to the peak value at the far right of the histogram [20]. $ref_2$ parameter is found via maximum entropy [5,21]:

$$H(I_{FDF}) = \frac{1}{MxN} \sum_{j}^{N} \sum_{i}^{M} \mathrm{Entropy\,Type(T)}, \tag{4}$$

where $H(I_{FDF})$ value corresponds to the whole image and is obtained by using Norm entropy. Depending on the principle of maximum entropy, the value of entropy is directly proportional to the amount of contained information [21]. In the system, an ideal value of $ref_{2opt}$ is reached by checking all alternative values between $ref_1+1$ and $ref_3-1$. When the ideal $ref_2$ value is reached, the highest level of $H(I_{FDF})$ will be obtained. $H_{max}$ can be obtained with the help of the Eq. (4) [5,20] and the $ref_{2opt}$ value as follows:

$$H_{\max}\ (I_{FDF},\ ref_1,\ ref_2,\ ref_3) = \max\ \left\{H(I_{AF};\ ref_1,\ ref_2,\ ref_3) \mid r_{\min}\ \le ref_1 \le ref_{2opt} \le ref_3 \le r_{\max}\ \right\}. \tag{5}$$

After T subset is calculated, Eq. (6) is used to calculate F value.

$$F = 1 - T. \tag{6}$$

The process mentioned above is summarized in Algorithm 1. The images of T and F subsets obtained at the end of this process are shown in Fig. 4.

Please cite this article as: E. Sert, A new modified neutrosophic set segmentation approach, Computers and Electrical Engineering (2017), http://dx.doi.org/10.1016/j.compeleceng.2017.01.017

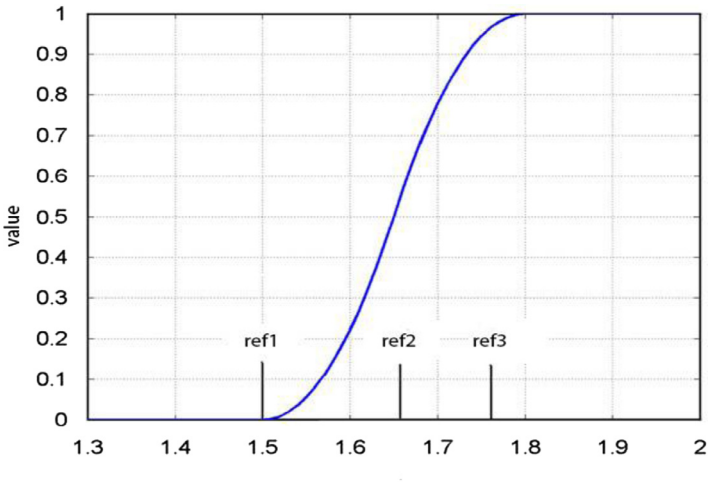


**Fig. 3.** Shape of the S-function.

**Algorithm 1**
The process in which T and F subsets are obtained.

$H_{max}$ = - Infinity
bopt = $ref_1$+1
for $ref_2$=$ref_1$+1:$ref_3$-1
  T = S_func($I_{FDF}$,$ref_1$,$ref_2$,$ref_3$)
  H = Norm Entropy (T)
  if H > $H_{max}$
    $H_{max}$ = H
    $ref_{2opt}$ = $ref_2$
  end
end
$ref_2$ = $ref_{2opt}$
T = S_func ($I_{FDF}$, $ref_1$, $ref_2$, $ref_3$);
F = 1 - T

a) T Subset Image b) Binary T subset image c) F subset image

d) Binary F subset image

**Fig. 4.** Original image and analysis results.

Please cite this article as: E. Sert, A new modified neutrosophic set segmentation approach, Computers and Electrical Engineering (2017), http://dx.doi.org/10.1016/j.compeleceng.2017.01.017

*2.2.3. Entropy norm*

Entropy is based on the probability theory and used extensively in the field of epistemology. It is a useful concept used for the calculation of amount of knowledge in various fields such as image processing, signal processing and so forth. It can be defined as Eq. (7) in general form [22].

$$H\ (\ Y\ ) = \ -\ \sum_{i=1}^{m} s_i\ log_2\ s_i\ , \tag{7}$$

where Y is a randomly chosen variable. When $s_i = 0$, the value of $0\log_2 0$ is 0, and H (Y) represents indeterminacy value. H, which defines entropy value, corresponds to the average value of knowledge when Y value is known [22]. There are various types of entropy such as Shannon entropy, threshold entropy, Sure entropy, log energy entropy and norm entropy. Norm entropy was preferred for this study because it yields the most successful segmentation performance. The Norm entropy $H_N$ (s) is defined as follows:

$$H_M(Y) = \sum_{i=0}^{m} |Y_i|^p,\ for\ 1 \le p < 2, \tag{8}$$

where Y is a signal, and $Y_i$ is the component of Y variable.

*2.2.4. The determination of $T_{ST}$ and $T_{SF}$ thresholds*

$T_{ST}$ and $T_{SF}$ parameters are used for objects (OB), edges (ED) and background (BG) to be obtained during the segmentation process. Otsu's adaptive thresholding [12,13] method is used in order to successfully obtain these values. It is a clustering based method used to calculate optimal threshold value that automatically separates object and background [12,13]. The method is detailed in [12]. In Otsu's method, the threshold value obtained by using T subset as input image is called $T_{ST}$, and the threshold parameter obtained by using F subset is called $T_{SF}$.

*2.2.5. Obtaining I*

A five-stage algorithm based on the study of Zhang et al. [5] is used to find I. It consists of the following steps:

(i) Calculate the average of the intensity values to measure d**x**d as:

$$mean\_int(i,\ j) = \frac{\sum_{k=i-(d-1)/2}^{i+(d-1)/2} \sum_{l=j-(d-1)/2}^{j+(d-1)/2} I_{FDF}(\mathrm{k},\ \mathrm{l})}{d^2}, \tag{9}$$

where $(I_{FDF})$ (k, l) is intensity value of pixel (i, j) of the d**x**d sized image to be analyzed for the mean.

(ii) Standard deviation is an important tool to define the contrast degree of pixels. The standard deviation of the image in (i, j) coordinates are calculated as follows:

$$st\_dev(i,\ j) = \sqrt{\frac{\sum_{k=i-(d-1)/2}^{i+(d-1)/2} \sum_{l=j-(d-1)/2}^{j+(d-1)/2} \left(I_{FDF}\ (\mathrm{k},\ \mathrm{l}) - mean\_int_{ij}\ \right)^2}{d^2}}, \tag{10}$$

where a size d**x**d window centered at (x, y) is used for st_dev.

(iii) The discontinuity of pixel D is calculated using Sobel operator:

$$S_{dsc}(i,\ j) = \sqrt{T_i^2 + T_j^2}, \tag{11}$$

where $T_i$ and $T_j$ are horizontal and vertical derivative approaches, respectively.

(iv) Homogenity (H) is related to local information and increases during object and background [3]. The value of H(i,j) is calculated as follows:

$$H(i,\ j) = 1 - \frac{st\_dev\ (i,\ j)}{st\_dev_{max}} - \ \frac{s\_dsc\ (i,\ j)}{S_{dscmax}}, \tag{12}$$

where $st\_dev_{max}$ is equal to (st_dev(i, j)), and $S_{dscmax}$ is equal to max(s_dsc (i, j)).

(v) Finding I(i,j):

$$I(i,\ j) = 1 - H(i,\ j), \tag{13}$$

H and I subset images obtained at the end of this process are shown in Figs. 5(a) and (b), respectively.

Please cite this article as: E. Sert, A new modified neutrosophic set segmentation approach, Computers and Electrical Engineering (2017), http://dx.doi.org/10.1016/j.compeleceng.2017.01.017

a) H subset image b) I subset image

**Fig. 5.** H and I images.

## 3. Segmentation

### 3.1. MNSS algorithm

In this step, objects (OB), edges (ED) and the background (BG) are determined by using the $T_{ST}$, $T_{SF}$, $T_{SI}$, $T$, $I$, and $F$. Then, the Binary NS image ($I_{BNS}$) is obtained. The method and mathematical equations in Zhang et al. [5] were used to calculate OB, ED, BG and $I_{BNS}$. Similar to the approach in [5], OB, ED, and BG are defined by:

$$OB(i,j) = \begin{cases} \text{true} & T(i,j) \geq T_{ST} \text{ and } I(i,j) < T_{SI}, \\ \text{false} & \text{others}, \end{cases} \tag{14}$$

$$D(i,j) = \begin{cases} \text{true} & (T(i,j) < T_{ST} \text{ or } F(i,j) < T_{SF}) \text{ and } I(i,j) \geq T_{SI}, \\ \text{false} & \text{others}, \end{cases} \tag{15}$$

$$BG(i,j) = \begin{cases} \text{true} & F(i,j) \geq T_{ST} \text{ and } I(i,j) < T_{SI} \\ \text{false} & \text{others}, \end{cases} \tag{16}$$

where $T_{SI}$ is set to 0.05 for all analyses. After OB, ED and BG are found, the $I_{BNS}$ [5] is obtained as:

$$I_{BNS} = (OB) \text{ or } (ED) \text{ or } \overline{BG(i,j)}$$
$$I_{BNS}(i,j) = \begin{cases} 1 & OB(i,j) \text{ or } ED(i,j) \text{ or } \overline{BG(i,j)} = \text{true} \\ 0 & \text{false} \end{cases} \tag{17}$$

After obtaining $I_{BNS}$, the segmentation of the object(s) is performed using the following steps:

**Step 1:** Calculate the complement of $I_{BNS}$ to get $\overline{I_{BNS}}$
**Step 2:** Do a morphological opening operation to $\overline{I_{BNS}}$
**Step 3:** Fill in the gaps in $\overline{I_{BNS}}$.
**Step 4:** Complement $\overline{I_{BNS}}$ to obtain the segmentation result.
**Step 5:** Name $I_{BNS}$ as NS Segmentation Image ($I_{NSS}$).

$I_{BNS}$ and $I_{NSS}$ are given in Fig. 6.

### 3.2. OATS algorithm

In OATS approach, input image in gray format is converted to binary format depending on global threshold [12] value after it is processed via this method. Accordingly, $I_{FDF}$ image is converted to grey format in the first step and segmented via OATS algorithm to obtain OATS image ($I_{OATS}$) as shown in Fig. 7(a) which is used in OATS based 3D modeling system.

### 3.3. FCMS algorithm

Fuzzy C-Means (FCM) algorithm introduced by Bezdek aims to divide 1 into Cluster C via iteratively minimizing objective function as follows [14]:

$$J_M = \sum_{t=1}^{c} \sum_{i=1}^{S} u_{ti}^{m} || l_i - h_t ||^2, \tag{18}$$

Please cite this article as: E. Sert, A new modified neutrosophic set segmentation approach, Computers and Electrical Engineering (2017), http://dx.doi.org/10.1016/j.compeleceng.2017.01.017

a) $I_{BNS}$ image b) $I_{NSS}$ image

**Fig. 6.** The analysis result images.

a) $I_{OATS}$ image b) $I_{FCMS}$ image

**Fig. 7.** Segmentation images.

where $l = \{l_1, l_2, \ldots, l_N\}$ corresponds to an image with pixel S, and m is the weighing exponent on each fuzzy member. $h_t$ is the $h$th cluster center, and $u_{ti}$ defines the membership degree of $i_{th}$ pixel corresponding to $h$th cluster created via $\sum_{t=1}^{S} u_{ti} = 1$. Membership $u_{ti}$ and the cluster centers $h_t$ are updated by:

$$u_{ti} = \frac{1}{\sum_{j=1}^{c} \left( \left( \frac{|| l_i - h_t ||}{|| l_i - h_j ||} \right)^{\frac{2}{(m-1)}} \right)}, \tag{19}$$

$$v_k = \frac{\sum_{i=1}^{S} u_{ti}^m l_i}{\sum_{i=1}^{S} u_{ti}^m}, \tag{20}$$

FCM Segmentation Image ($I_{FCMS}$), which is obtained by segmenting $I_{FDF}$ image via FCM algorithm, is shown in Fig. 7(b). This image will be used in FCMS based 3D modeling system.

## 4. 3D modeling

### *4.1. 3D modeling method via MNSS (3DMM_MNSS)*

In the first step, preprocessing of the original image is performed. In the second step, the segmentation with the MNSS is performed. In the last step, 3D model is obtained by using the depth map, the segmented image and the original image. The flow diagram of the proposed 3DMM_MNSS system is shown in Fig. 8.

Depth information in the depth map, which is of vital importance in 3D modeling, is stored within a grayscale value of between 0 and 255. When the surface becomes distant, its color equivalent converges to black in depth map because the grayscale value decreases. When the surface becomes closer, its color equivalent converges to white in depth map because the grayscale value increases. An example of a depth map and its grayscale value band are shown in Fig. 9.

The operational steps of 3D modeling are summarized in Algorithm 2. Because the 3D model to be created is in ply format, the header settings were adjusted at the beginning of the algorithm. In the related algorithm, 3D Model variable is obtained depending on color, xpos (x position), ypos (y position) and zpos (z position) and $I_{NSS}$ variables. 3D Model variable is shown in Fig. 10(a).

Please cite this article as: E. Sert, A new modified neutrosophic set segmentation approach, Computers and Electrical Engineering (2017), http://dx.doi.org/10.1016/j.compeleceng.2017.01.017

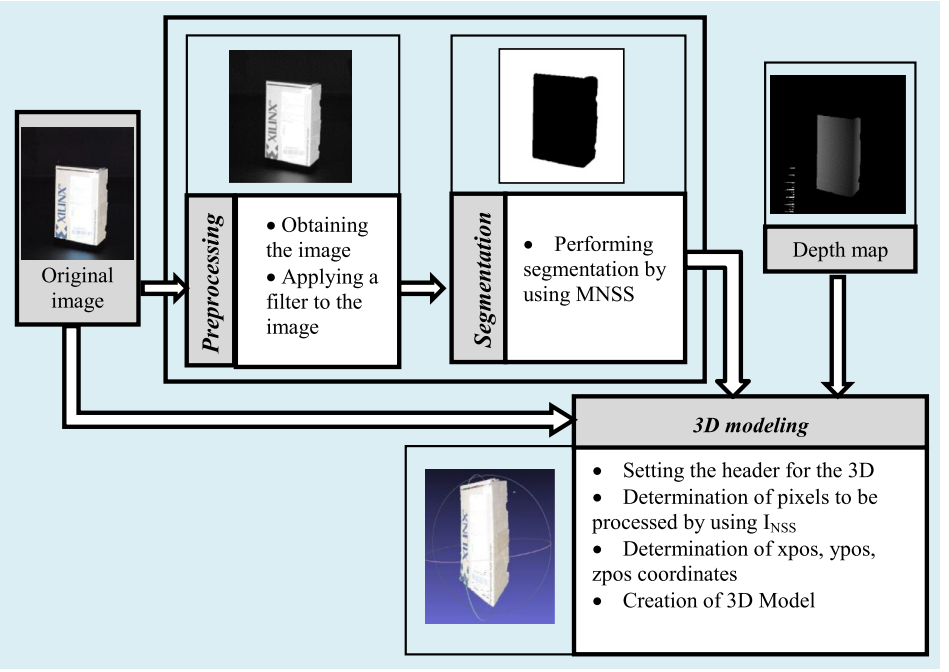


**Fig. 8.** 3D modeling system flow diagram.

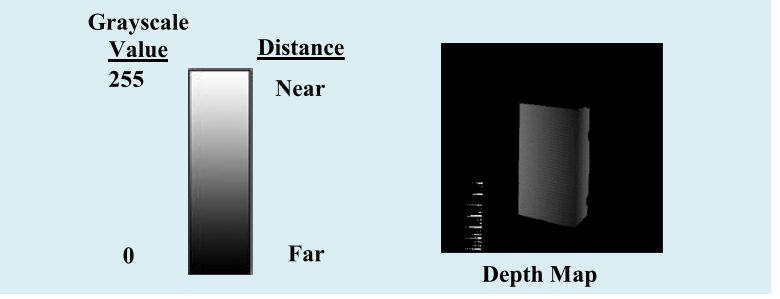


**Fig. 9.** Depth map information.

**Algorithm 2**
The steps in creating 3D model.

```
1. The creation of the header information for 3D modeling in PLY format
2. for j = 0 to Height of Original Image
3.    for i = 0 to Width of Original Image
4.         color(i,j) ← Original Image (i, j)
5.         xPos = j / Height of Original Image
6.         yPos = 1 -i / Width of Original Image
7.         zPos = 1 - (Depth Map [i, j] / 255)
8.         IF I_NSS (i,j) = True 3D Model (xpos, ypos, zpos) = Color (x,y)
9.     end i
10. end j
11. end of ply files
```

### 4.2. 3D modeling method via OATS (3DMM_OATS)

Similar to 3DMM_MNSS, 3DMM_OATS benefits from $I_{OATS}$, original image and depth map for modeling. 3D modeling is carried out via the algorithmic process obtained as a result of using $I_{OATS}$ instead of $I_{NSS}$ in the 8th line of Algorithm 2. 3D model obtained via this approach is shown in Fig. 10(b).

Please cite this article as: E. Sert, A new modified neutrosophic set segmentation approach, Computers and Electrical Engineering (2017), http://dx.doi.org/10.1016/j.compeleceng.2017.01.017

a) 3D model obtained by b) 3D model obtained by c) 3D model obtained by

**Fig. 10.** 3D models.

### 4.3. 3D modeling method via FCMS (3DMM_FCMS)

Similar to 3DMM_MNSS, 3DMM_FCMS uses $I_{FCMS}$, original image and depth map for modeling. 3D modeling with FMCS is carried out via the algorithmic process obtained as a result of using $I_{FCMS}$ instead of $I_{NSS}$ in the 8th line of Algorithm 2. 3D model obtained via this approach is shown in Fig. 10(c).

## 5. Experiments

### 5.1. Evaluation of segmentation performance

Metric Figure of Merit (FOM) introduced by Pratt [23], Peak Signal-To-Noise Ratio (PSNR) [24] and Uniformity Measure (UM) [25] measurements are commonly used for the quantitative performance comparison of the segmentation images. Accordingly, FOM, PSNR and UM tests were carried out on $I_{NSS,}$ $I_{OATS}$ and $I_{FCMS}$ images.

In FOM analysis, which is commonly used to measure the segmentation performance, the result equals to 1 for the best edge detection result, while this parameter converges to 0 in case of a poor performance. This analysis is based on Eq. (21).

$$FOM = \frac{1}{\max(EI_D, EI_A)} \sum_{i=1}^{EDI_A} \frac{1}{1 + dm^2(i)}, \tag{21}$$

where $EI_D$ (Edge Image $_{Detected}$) corresponds to the number of the detected edge points, and $EI_A$ (Edge Image $_{Actual}$) corresponds to the number of real edge points. S is the size of the image, and m (i) parameter is the shortest distance to *i*th real edge. d parameter is used for scaling. The formulas given in Eqs. (22) and (23) are used for the analysis of PSNR. Mean Square Error (MSE) [24] is calculated as follows:

$$\text{MSE} = \sum_{i,j=1}^{S} \frac{[OI(i,j) - SI(i,j)]}{S^2}, \tag{22}$$

where OI is the original image, and SI is segmented image. S is the size of OI. Eq. (23) is used to find PSNR. The value of PSNR is direclty proportional to the quality of segmentation.

$$PSNR = 10\ log_{10}\left(\frac{255^2}{MSE}\right). \tag{23}$$

Regularity in the segmented image is one of the most important tools to measure the quality of segmentation. To this aim, Uniformity Measure (UM) was used in the study. UM is calculated as follows:

$$UM = 1 - \frac{1}{k}\sum_{x}\left\{\sum_{(i,j)\in Reg_x}\left[SI(i,j) - \frac{1}{sz_i}\sum_{(i,j)\in Reg_x} SI(i,j)\right]^2\right\}, \tag{24}$$

where k is the optimization parameter ensuring the UM results in between 0 and 1. $Reg_x$ refers to *x*th segmented area, and $sz_i$ refers to the size of $Reg_x$. SI(i,j) is the value of SI image in the (i,j) coordinate.

$I_{NSS}$, $I_{OATS}$ and $I_{FCMS}$ images of 20 boxes with different sizes obtained via MNSS, OATS and FCMS algorithms were tested in this process. 3D modeling results obtained via three methods are shown in Fig 11. In the first run, FOM, PSNR and UM tests were carried out on $I_{NSS}$, $I_{OATS}$ and $I_{FCMS}$ in Fig 11. The obtained test results are given in **Test no. 1** in Table 1. In second run, same tests are applied for $I_{NSS}$, $I_{OATS}$ and $I_{FCMS}$ images in Fig. 12. The test results obtained at the end of this process are presented in **Test no. 2** in Table 1.

Please cite this article as: E. Sert, A new modified neutrosophic set segmentation approach, Computers and Electrical Engineering (2017), http://dx.doi.org/10.1016/j.compeleceng.2017.01.017

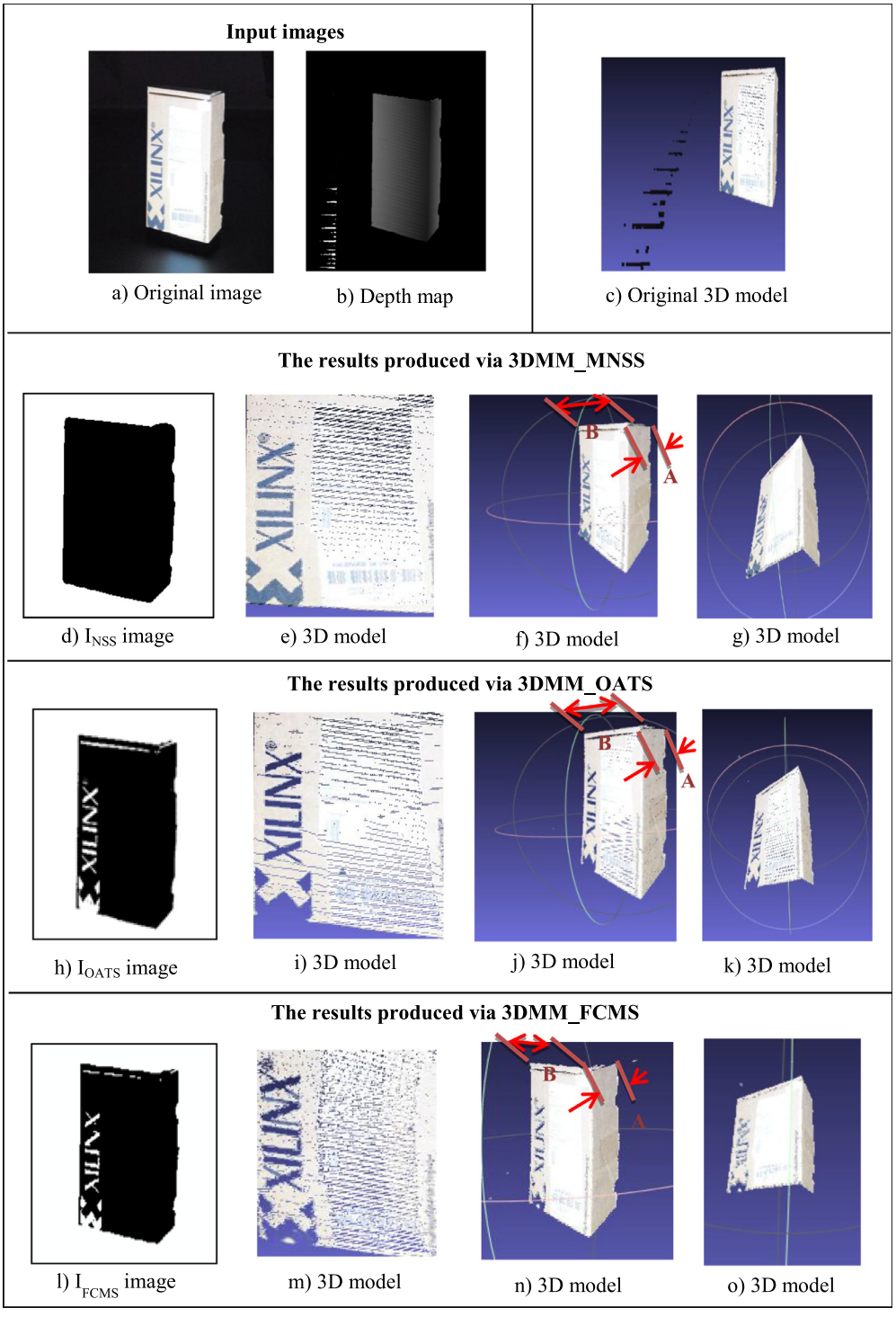


**Fig. 11.** The input images and obtained results.

In addition to the testing performed on 2 different objects given in detail above, 18 $I_{NSS}$, $I_{OATS}$ and $I_{FCMS}$ images were obtained by applying three segmentation methods to 18 boxes with different sizes. The results of FOM, PSNR and UM tests carried out on the images in order to measure the segmentation performances of these three methods are given between **Test no. 3** – **Test no. 20** in Table 1. The results of 20 tests demonstrate that FOM, PSNR and UM results obtained with the MNSS are at a higher level than other methods.

Please cite this article as: E. Sert, A new modified neutrosophic set segmentation approach, Computers and Electrical Engineering (2017), http://dx.doi.org/10.1016/j.compeleceng.2017.01.017

**Table 1**
PSNR, FOM and UM analysis results.

| | For $I_{NSS}$ images | | | For $I_{OATS}$ images | | | For $I_{FCMS}$ images | | |
|---|---|---|---|---|---|---|---|---|---|
| Test no. | PSNR results (dB) | UM results | FOM results | PSNR results (dB) | UM results | FOM results | PSNR results (dB) | UM results | FOM results |
| 1 | 32,96 | 0,93 | 0,95 | 24,74 | 0,69 | 0,67 | 27,54 | 0,78 | 0,76 |
| 2 | 33,42 | 0,95 | 0,94 | 24,01 | 0,68 | 0,66 | 20,45 | 0,58 | 0,57 |
| 3 | 30,45 | 0,88 | 0,90 | 24,65 | 0,67 | 0,68 | 25,34 | 0,73 | 0,71 |
| 4 | 32,08 | 0,91 | 0,90 | 23,98 | 0,65 | 0,67 | 25,23 | 0,72 | 0,70 |
| 5 | 31,88 | 0,91 | 0,88 | 24,75 | 0,71 | 0,69 | 23,21 | 0,66 | 0,66 |
| 6 | 30,87 | 0,89 | 0,92 | 22,65 | 0,63 | 0,65 | 26,76 | 0,76 | 0,74 |
| 7 | 29,99 | 0,86 | 0,88 | 22,78 | 0,64 | 0,66 | 26,34 | 0,76 | 0,78 |
| 8 | 27,54 | 0,79 | 0,83 | 21,54 | 0,61 | 0,62 | 25,87 | 0,74 | 0,72 |
| 9 | 31,01 | 0,89 | 0,88 | 23,78 | 0,65 | 0,64 | 22,43 | 0,64 | 0,66 |
| 10 | 29,99 | 0,86 | 0,88 | 22,65 | 0,64 | 0,64 | 21,54 | 0,62 | 0,61 |
| 11 | 33,99 | 0,97 | 0,96 | 23,8 | 0,67 | 0,65 | 26,65 | 0,76 | 0,74 |
| 12 | 31,88 | 0,90 | 0,88 | 23,65 | 0,65 | 0,66 | 23,54 | 0,67 | 0,67 |
| 13 | 29,98 | 0,86 | 0,85 | 19,87 | 0,57 | 0,59 | 21,34 | 0,61 | 0,63 |
| 14 | 29,65 | 0,85 | 0,87 | 21,14 | 0,62 | 0,61 | 26,28 | 0,75 | 0,73 |
| 15 | 30,87 | 0,87 | 0,85 | 22,01 | 0,62 | 0,60 | 25,14 | 0,72 | 0,71 |
| 16 | 29,67 | 0,83 | 0,83 | 21,68 | 0,63 | 0,61 | 21,12 | 0,59 | 0,56 |
| 17 | 30,23 | 0,87 | 0,85 | 22,45 | 0,65 | 0,64 | 25,87 | 0,74 | 0,77 |
| 18 | 31,76 | 0,91 | 0,92 | 22,64 | 0,66 | 0,67 | 27,34 | 0,79 | 0,78 |
| 19 | 31,54 | 0,91 | 0,89 | 21,75 | 0,63 | 0,65 | 26,87 | 0,77 | 0,76 |
| 20 | 29,78 | 0,85 | 0,86 | 22,97 | 0,66 | 0,67 | 25,55 | 0,73 | 0,71 |

The graphical representations of FOM, PSNR and UM results are shown in Fig. 13. It is observed in these three graphs that the FOM, PSNR and UM results of $I_{NSS}$ Image are higher than the other two images. The test results given in Table 1 are statistically analyzed, and the results are given in Table 2. The statistical results demonstrate that maximum, minimum and arithmetic mean of FOM, PSNR and UM results for $I_{NSS}$ images are higher than $I_{OATS}$ and $I_{FCMS}$ images. These results demonstrate the superiority of MNSS over OATS and FCMS.

### 5.2. Comparison and size measurement analysis on 3D models

$I_{NSS}$, $I_{OATS}$ and $I_{FCMS}$ images of 20 boxes obtained in the previous testing process and depth maps of these boxes are processed via 3DMM_MNSS, 3DMM_OATS and 3DMM_FCMS for 3D modeling. These 3D models were used for visual comparison and size measurements. In addition, error analysis was performed on size measurements. The first test was carried out on 3D models in Fig. 11, and test process and results are summarized below.

The image in Fig. 11(c) was obtained as a result of a direct 3D modeling with the original image in Fig. 11(a) and the depth map in Fig. 11(b). Because of the existing depth information in the parts that do not belong to the object in the depth map in Fig. 11(b), unintended black images occurred in different locations of three dimensional plane in 3D model in Fig. 11(c), which decreased the quality of 3D modeling. It can be noted that 3D model obtained with the **3DMM_MNSS** and other methods eliminated this problem.

3D modeling results obtained via the 3DMM_MNSS are shown in Fig. 11(e)–(g). As shown in the $I_{NSS}$ image in Fig. 11(d), the parts with the black logo and text on the box are perceived to be holistically involved in the box and segmented with the box. Because the $I_{NSS}$ image is used in the determination of the object regions to be modeled, the parts with the black logo and text on the box are successfully modeled as shown in Fig. 11(e)–(g).

The logo and text on the box could not be holistically segmented as shown in $I_{OATS}$ image in Fig. 11(h) and $I_{FCMS}$ image in Fig. 11(l). As a result, the related parts could not be modeled and thus remained empty in 3D modelings obtained via 3DMM_OATS and 3DMM_FCMS as shown in Fig. 11(i)–(k) and (m)–(o). The parts which could not be modeled can be clearly seen in Fig. 11(i) and m. Therefore, it can be concluded that the 3DMM_MNSS approach created 3D modeling much more successfully.

The dimensioning of 3D models obtained via the 3DMM_MNSS, 3DMM_OATS and 3DMM_FCMS are given in Fig. 11(f), (j) and (n), respectively. The real edge measurements of A and B, and the edge measurements of A and B obtained via three methods are given under **Test no. 1** in Table 3. Absolute error analysis ($\Delta$ae (Absolute Error)) given in Eq. (25) was performed on these edge measures. The results are also given under **Test no. 1** in Table 3.

$$\Delta ae = |\text{Real value} - \text{Measured Value}|, \tag{25}$$

Same testing process was repeated for 3D models in Fig. 12. Results of the edge measurements and the absolute error analysis are given **Test no. 2** in Table 3. Visual comparisons and $\Delta$ae results demonstrated that 3DMM_MNSS approach created 3D modeling much more successfully.

3D modelings of 18 boxes with different sizes used for the segmentation test in the previous sub-section were performed via 3DMM_MNSS, 3DMM_OATS and 3DMM_FCMS depending on the same rank with **Test no.** presented in Table 1. The results of the edge measurement and $\Delta$ae analysis obtained for 18 additional images are given between **Test no. 3** and **Test**

Please cite this article as: E. Sert, A new modified neutrosophic set segmentation approach, Computers and Electrical Engineering (2017), http://dx.doi.org/10.1016/j.compeleceng.2017.01.017

**Table 2**
Statistical results.

| | For $I_{NSS}$ images | | | For $I_{OATS}$ images | | | For $I_{FCMS}$ images | | |
|---|---|---|---|---|---|---|---|---|---|
| | Statistical results for PSNR (dB) | Statistical results for UM | Statistical results for FOM | Statistical results for PSNR (dB) | Statistical results for UM | Statistical results for FOM | Statistical results for PSNR (dB) | Statistical results for UM | Statistical results for FOM |
| Maximum | 33,99 | 0,97 | 0,96 | 24,75 | 0,71 | 0,69 | 27,54 | 0,79 | 0,78 |
| Minimum | 27,54 | 0,79 | 0,83 | 19,87 | 0,57 | 0,59 | 20,45 | 0,58 | 0,56 |
| Arithmetic mean | 30,98 | 0,88 | 0,89 | 22,87 | 0,65 | 0,65 | 24,72 | 0,71 | 0,70 |

Please cite this article as: E. Sert, A new modified neutrosophic set segmentation approach, Computers and Electrical Engineering (2017), http://dx.doi.org/10.1016/j.compeleceng.2017.01.017

**Table 3**
Size measurements and calculated Δae results.

| | Actual edge measures (cm) | | The results of the measurement performed on the 3D model obtained via the 3DMM_MNSS | | | | The results of the measurement performed on the 3D model obtained via 3DMM_OATS | | | | The results of the measurement performed on the 3D model obtained via 3DMM_FCMS | | | |
|---|---|---|---|---|---|---|---|---|---|---|---|---|---|---|
| Test no. | A (cm) | B (cm) | A (cm) | Δae for A | B (cm) | Δae for B (cm) | A (cm) | Δae for A (cm) | B (cm) | Δae for B (cm) | A (cm) | Δae for A (cm) | B (cm) | Δae for B (cm) |
| 1 | 9,76 | 21,43 | 9,80 | 0,04 | 21,68 | 0,25 | 9,57 | 0,19 | 21,01 | 0,42 | 9,71 | 0,05 | 21,12 | 0,31 |
| 2 | 34,67 | 35,23 | 35,08 | 0,41 | 35,67 | 0,44 | 33,97 | 0,70 | 34,52 | 0,71 | 33,85 | 0,82 | 34,42 | 0,81 |
| 3 | 5,81 | 5,81 | 5,87 | 0,06 | 5,87 | 0,06 | 5,70 | 0,11 | 5,71 | 0,10 | 5,72 | 0,09 | 5,73 | 0,08 |
| 4 | 10,23 | 6,78 | 10,31 | 0,08 | 6,85 | 0,07 | 10,02 | 0,21 | 6,65 | 0,13 | 10,12 | 0,11 | 6,68 | 0,10 |
| 5 | 7,32 | 12,23 | 7,41 | 0,09 | 12,39 | 0,16 | 7,18 | 0,14 | 11,97 | 0,26 | 7,05 | 0,27 | 11,91 | 0,32 |
| 6 | 8,15 | 14,00 | 8,24 | 0,09 | 14,17 | 0,17 | 7,99 | 0,16 | 13,71 | 0,29 | 8,02 | 0,13 | 13,79 | 0,21 |
| 7 | 4,31 | 6,54 | 4,32 | 0,01 | 6,62 | 0,08 | 4,22 | 0,09 | 6,40 | 0,14 | 4,24 | 0,07 | 6,42 | 0,12 |
| 8 | 24,34 | 10,23 | 24,61 | 0,27 | 10,34 | 0,11 | 23,86 | 0,48 | 10,02 | 0,21 | 24,01 | 0,33 | 10,07 | 0,16 |
| 9 | 12,76 | 30,14 | 12,93 | 0,17 | 30,52 | 0,38 | 12,50 | 0,26 | 29,54 | 0,60 | 12,28 | 0,48 | 29,34 | 0,80 |
| 10 | 13,34 | 27,34 | 13,47 | 0,13 | 27,70 | 0,36 | 13,08 | 0,26 | 26,80 | 0,54 | 12,89 | 0,45 | 26,71 | 0,63 |
| 11 | 13,54 | 26,23 | 13,69 | 0,15 | 26,51 | 0,28 | 13,27 | 0,27 | 25,70 | 0,53 | 13,31 | 0,23 | 25,79 | 0,44 |
| 12 | 29,54 | 13,76 | 29,90 | 0,36 | 13,95 | 0,19 | 28,97 | 0,57 | 13,48 | 0,28 | 28,95 | 0,59 | 13,41 | 0,35 |
| 13 | 14,86 | 32,14 | 15,02 | 0,16 | 32,51 | 0,37 | 14,58 | 0,28 | 31,51 | 0,63 | 14,61 | 0,25 | 31,68 | 0,46 |
| 14 | 15,00 | 23,25 | 15,07 | 0,07 | 23,56 | 0,31 | 14,70 | 0,30 | 22,78 | 0,47 | 14,92 | 0,08 | 22,88 | 0,37 |
| 15 | 16,01 | 30,12 | 16,06 | 0,05 | 30,49 | 0,37 | 15,68 | 0,33 | 29,52 | 0,60 | 16,07 | 0,06 | 29,68 | 0,44 |
| 16 | 25,34 | 17,11 | 25,61 | 0,27 | 17,33 | 0,22 | 24,84 | 0,50 | 16,77 | 0,34 | 24,74 | 0,60 | 16,71 | 0,40 |
| 17 | 17,55 | 40,76 | 17,78 | 0,23 | 41,25 | 0,49 | 17,20 | 0,35 | 39,95 | 0,81 | 17,25 | 0,30 | 40,24 | 0,52 |
| 18 | 5,11 | 6,76 | 5,16 | 0,05 | 6,83 | 0,07 | 5,00 | 0,11 | 6,63 | 0,13 | 5,03 | 0,08 | 6,68 | 0,08 |
| 19 | 30,23 | 19,05 | 30,61 | 0,38 | 19,30 | 0,25 | 29,63 | 0,60 | 18,66 | 0,39 | 29,77 | 0,46 | 18,69 | 0,36 |
| 20 | 20,23 | 35,45 | 20,49 | 0,26 | 35,91 | 0,46 | 19,83 | 0,40 | 34,75 | 0,70 | 19,92 | 0,31 | 34,85 | 0,60 |

Please cite this article as: E. Sert, A new modified neutrosophic set segmentation approach, Computers and Electrical Engineering (2017), http://dx.doi.org/10.1016/j.compeleceng.2017.01.017

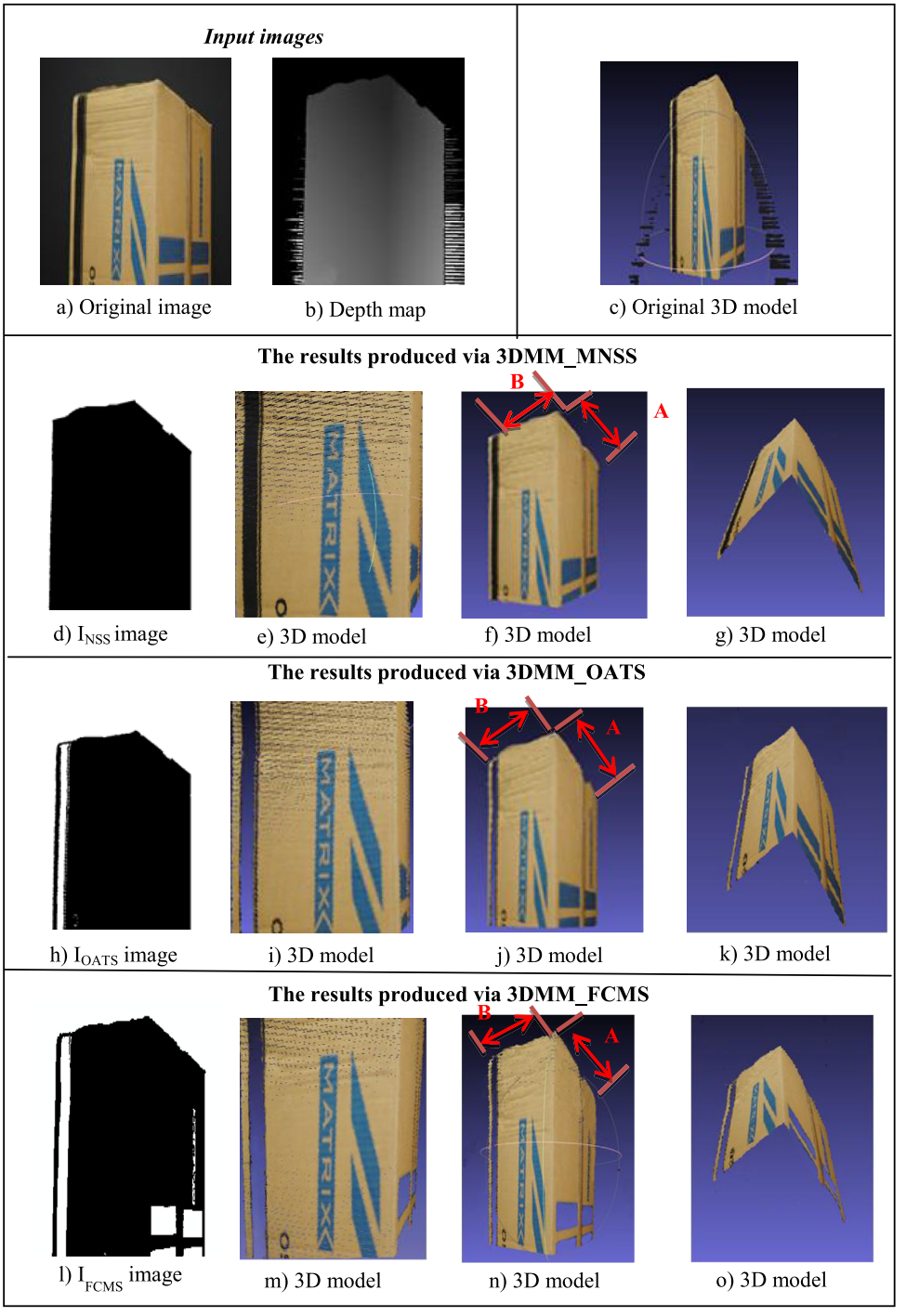


**Fig. 12.** The input images and obtained results.

**no. 20** in Table 3 respectively. Statistical analyses were performed on $\Delta ae$'s in Table 3, and the obtained results are given in Table 4. The analysis results demonstrate that the maximum, minimum and average values of $\Delta ae$ results obtained via the 3DMM_MNSS are at a lowest compared to two other methods. Therefore, it is proved based on the results that the edges of the object were modeled more realistically via the 3DMM_MNSS. In addition, visual comparisons performed on 3D models demonstrated superiority of the 3DMM_MNSS method over OATS and FCMS methods.

Please cite this article as: E. Sert, A new modified neutrosophic set segmentation approach, Computers and Electrical Engineering (2017), http://dx.doi.org/10.1016/j.compeleceng.2017.01.017

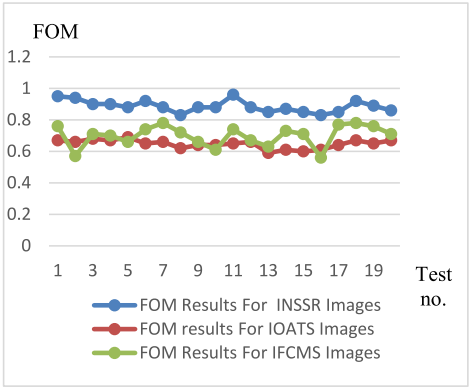


a) Graph of FOM results

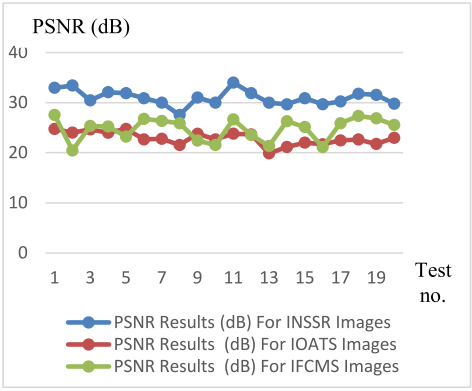


b) Graph of PSNR results

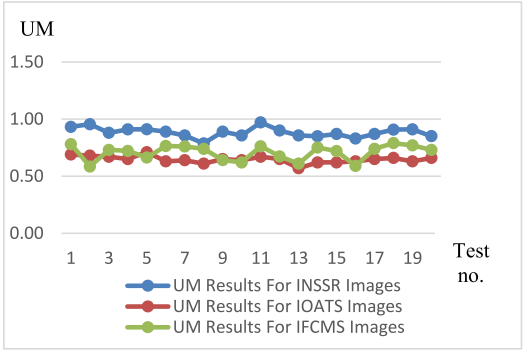


c) Graph of UM results

**Fig. 13.** Graphs of test results.

**Table 4**
Statistical results.

| | The proposed approach | | 3DMM_OATS | | 3DMM_FCMS | |
|---|---|---|---|---|---|---|
| | Δae for A (cm) | Δae for B (cm) | Δae for A (cm) | Δae for B (cm) | Δae for A (cm) | Δae for B (cm) |
| Maximum | 0,41 | 0,49 | 0,7 | 0,81 | 0,82 | 0,81 |
| Minimum | 0,01 | 0,06 | 0,09 | 0,1 | 0,05 | 0,08 |
| Arithmetic mean | 0,16 | 0,25 | 0,31 | 0,41 | 0,28 | 0,37 |

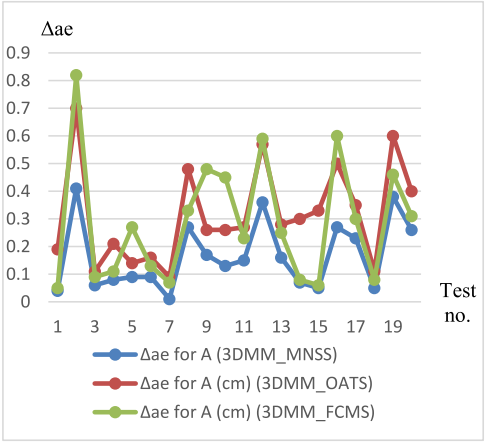


a) Graphical representation of Δae results for the measurement of distance A via the three methods

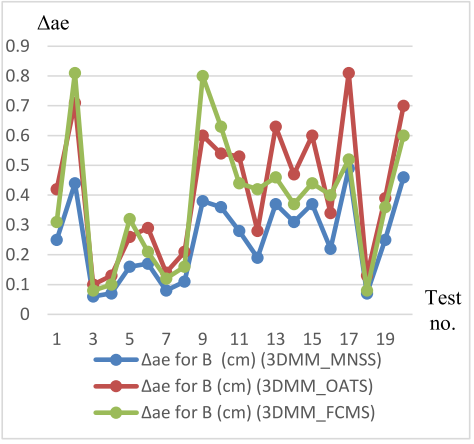


b) Graphical representation of Δae results for the measurement of distance B via the three methods

**Fig. 14.** Graphical representations.

Please cite this article as: E. Sert, A new modified neutrosophic set segmentation approach, Computers and Electrical Engineering (2017), http://dx.doi.org/10.1016/j.compeleceng.2017.01.017

Graphical representations of Δae results obtained via the 3DMM_MNSS, 3DMM_OATS and 3DMM_FCMS given in Table 3 are presented in Fig. 14. Obtained Δae results demonstrate that 3DMM_MNSS gives lowest error rates compared to other methods.

## 6. Conclusion

NS is a successful technique which has been recently used in segmentation studies. An image is converted to three subsets as T, I and F depending on the NS approach. MNSS was proposed by using Norm Entropy in NS-based segmentation method. This entropy was preferred in this study due to its success in the experimental studies. Additionally, the fractional derivative filter was used during the preprocessing phase in order to improve segmentation performance. $T_{ST}$, $T_{SF}$, $T_{SI}$, $T$, $I$, and $F$ were used in MNSS algorithm to find OB, ED and BG, and later $I_{BNS}$ and $I_{NSS}$ were obtained.

FOM, PSNR and UM were used to test the segmentation performances of the images obtained via MNSS, OATS and FCMS. MNSS is compared with OATS and FCMS by these tests. The arithmetic mean of PSNR, UM and FOM for $I_{NSS}$ images obtained via MNSS algorithm on 20 test images were 30.98, 0.88 and 0.89, respectively. These results indicate the superiority of MNSS approach. In 3DMM_MNSS approach, the depth map, $I_{NSS}$ and the original image were used to obtain 3D model. Thus, any potential problems in the depth map are eliminated and 3D modeling of the intended object is performed. 3DMM_MNSS was compared with 3DMM_FCMS and 3DMM_OATS through visual comparisons and size measurements. Visual comparisons performed on 3D models demonstrated the superiority of the 3DMM_MNSS. Maximum, minimum and arithmetic mean values of Δae results obtained via 3DMM_MNSS are lowest compared to other two methods. These test results suggest that the 3DMM_MNSS performs 3D modeling more successfully compared to OATS and FCMS methods. 3DMM_MNSS can be used in future studies such as medical and other applications due to its superior performance.

## Supplementary materials

Supplementary material associated with this article can be found, in the online version, at doi:10.1016/j.compeleceng.2017.01.017.

## References

[1] Sert E, Taskin D, Alkan A. Three stepped calibration of structured light system with adaptive thresholding for 3D measurements. Optik - Int J Light Electron Optics 2015;126:5176-5181.
[2] Cheng HD, Guo Y, Zhang Y. A novel image segmentation approach based on neutrosophic set and improved fuzzy c-means algorithm. New Math Natural Comput 2011;07:155-171.
[3] Smarandache F. A unifying field in logics neutrosophic logic, neutrosophy, neutrosophic set, neutrosophic probability. American Research Press; 2003.
[4] Guo Y, Cheng HD. New neutrosophic approach to image segmentation. Pattern Recogn 2009;42:587–95.
[5] Zhang M, Zhang L, Cheng HD. A neutrosophic approach to image segmentation based on watershed method. Signal Process 2010;90:1510-1517.
[6] Koundal D, Gupta S, Singh S. Automated delineation of thyroid nodules in ultrasound images using spatial neutrosophic clustering and level set. Appl Soft Comput 2016;40:86–97.
[7] Alsmadi MK. A hybrid fuzzy C-means and neutrosophic for jaw lesions segmentation. Ain Shams Eng J 2016 In Press, Corrected Proof.
[8] Nguyen A, Le B. 3D point cloud segmentation: a survey, robotics, automation and mechatronics. In: 6th IEEE conference. RAM; 2013. p. 225–30.
[9] Theologou P, Pratikakis I, Theoharis T. A comprehensive overview of methodologies and performance evaluation frameworks in 3D mesh segmentation. Comput Vis Image Understand 2015;135:49-82.
[10] Ramey A, Malfaz M, Salichs MA. Fast 3D cluster tracking for a mobile robot using 2D techniques on depth images. Cybern Syst An Int J 2013;44:325-350.
[11] Verma H, Agrawal RK, Sharan A. An improved intuitionistic fuzzy C-means clustering algorithm incorporating local information for brain image segmentation. Appl Soft Comput 2016;46:543–57.
[12] Otsu N. A threshold selection method from gray-level histograms. IEEE Trans Syst Man Cybern 1979;9:62-66.
[13] Yuana X-C, Wua L-S, Peng Q. An improved Otsu method using the weighted object variance for defect detection. Appl Surface Sci 2015;349:472–84.
[14] Bezdek JC. Pattern recognition with fuzzy objective function algorithms. Kluwer Academic Publishers Norwell; 1981.
[15] Qi X, Liu B, Xu J. A neutrosophic filter for high-density salt and pepper noise based on pixel-wise adaptive smoothing parameter. J Vis Commun Image Represent 2016;36:1–10.
[16] Shan J, Cheng HD, Wang Y. A novel segmentation method for breast ultrasound images based on neutrosophic l-means clustering. Med Phys 2012;39:5669–82.
[17] Khanna S, Chandrasekaran V. Fractional derivative filter for image contrast enhancement with order prediction. In: International conference on image processing. IET; 2012. p. 1–6.
[18] Kumar M, Rawat TK. Optimal fractional delay-IIR filter design using cuckoo search algorithm'. ISA Trans 2015;59:39–54.
[19] He N, Wang J-B, Zhang L-L, Lu K. An improved fractional-order differentiation model for image denoising. Signal Process 2015;112:180–8.
[20] Cheng HD, Wang J, Shi X. Microcalcification detection using fuzzy logic and scale space approaches. Pattern Recog 2004;37:363-375.
[21] Cheng HD, Xu H. A novel fuzzy logic approach to contrast enhancement. Pattern Recog 2000;33:809-919.
[22] Avci E, Sengur A, Hanbay D. An optimum feature extraction method for texture classification. Expert Syst Appl 2009;36:6036–43.
[23] Pratt WK. Digital image processing. John Wiley & Sons; 1978.
[24] Shilpa S, Shyam L. An efficient cuckoo search algorithm based multilevel thresholding for segmentation of satellite images using different objective functions. Expert Syst Appl 2016;58:184-209.
[25] Levine MD, Nazif AM. Dynamic measurement of computer generated image segmentation. IEEE Trans Pattern Anal Machine Intell 1985;7:155–64.

**Eser Sert** received M.Sc. degree in 2010 and Ph.D. degree in 2013, all in Computer Engineering from Trakya University, Turkey. Currently he is Assistant Professor of Computer Engineering at Kahramanmaras Sutcu Imam University, Turkey. His research interests include 3D modeling system, image processing, computer vision, field programmable gate arrays (FPGA) and artificial intelligence.

Please cite this article as: E. Sert, A new modified neutrosophic set segmentation approach, Computers and Electrical Engineering (2017), http://dx.doi.org/10.1016/j.compeleceng.2017.01.017